

Thin-Film Lithium Tantalate Modulator Operating at High Optical Power

Haohua Wang, Ao Cui, Bin Chen, Ziliang Ruan, Changjian Guo,* Kaixuan Chen,* and Liu Liu*



Cite This: <https://doi.org/10.1021/acsphtronics.5c00159>



Read Online

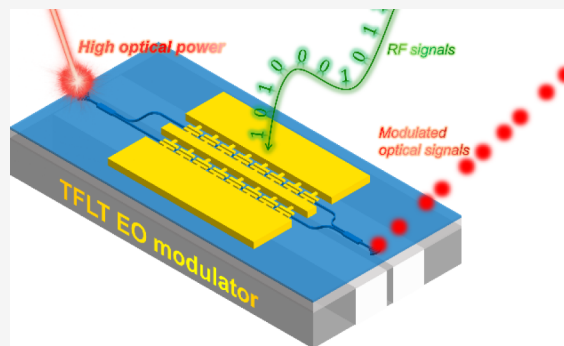
ACCESS |

Metrics & More

Article Recommendations

ABSTRACT: Handling high optical power in electro-optic modulators is critical for applications in nonlinear optics, microwave photonics, and THz communications. While thin-film lithium niobate (TFLN) modulators provide ultralarge bandwidth, their performance under high optical power is constrained by photorefractive (PR) effects. Thin-film lithium tantalate (TFLT) addresses this challenge with its significantly higher optical damage threshold and reduced PR effects, making it a promising material for high-power applications. In this work, we designed and experimentally demonstrated a high-performance TFLT modulator capable of stable operation at optical powers up to 28 dBm (630.9 mW). Compared to TFLN-based modulators, the TFLT device achieves enhanced stability and exhibits consistent high efficiency, low insertion loss, and large electro-optic bandwidth across various power levels. These results highlight the potential of TFLT modulators for next-generation high-power photonic systems.

KEYWORDS: lithium tantalate, electro-optic modulator, high optical power, photorefractive, optical damage, lithium niobate



INTRODUCTION

Thin-film lithium niobate (TFLN) electro-optic (EO) modulators have rapidly advanced in recent years, owing to their high modulation efficiency, large bandwidth, compact waveguides, and low loss.^{1–3} Several high-performance modulators have been reported, featuring EO bandwidths exceeding 110 GHz,⁴ half-wave voltages (V_{π}) below 1 V,⁵ or insertion losses (IL) under 0.2 dB.⁶ These devices are expected to be widely used in next-generation optical interconnects for data centers, coherent optical communications, and artificial intelligence computing.⁷ In these scenarios, high optical power is typically unnecessary, and modulators generally operate under relatively low power levels. However, certain applications—such as long-haul communications,⁸ nonlinear optics,⁹ microwave/mm-wave generation,^{10,11} THz communications,¹² and high-linearity analog photonic links^{12,13}—demand not only large bandwidth and high modulation efficiency but also the ability to handle high optical power. This capability is crucial for enhancing signal gain,^{10,14} mitigating third-order intermodulation,¹⁵ and reducing noise in RF photonic links.¹⁰ Unfortunately, undoped lithium niobate (LN), when exposed to high optical power, often suffers from severe photorefractive (PR) effects, leading to unstable operating points and even irreversible damage, such as deformation of the optical mode field distribution.^{15–19} This is reflected in its relatively low optical damage threshold (~1 kW/cm² @532 nm).²⁰ In a review paper, Zhang et al. predicted that TFLN modulators

could potentially handle watt-level optical power.²¹ However, this estimate was based solely on calculations from microring resonator waveguides, and actual power limits for modulators have yet to be theoretically modeled or experimentally demonstrated. Valdez et al. reported a Si-LN hybrid integrated EO modulator capable of handling optical power exceeding 110 mW, by mitigating the two-photon absorption limitations of silicon waveguides.²² However, their experiment was restricted to pulsed light operation, leaving the performance under higher continuous-wave optical power unclear. Doping LN with ZrO₂ or MgO^{23–25} has been shown to mitigate PR effects and increase the optical damage threshold. High-performance MgO-doped TFLN modulators have been demonstrated within the visible to near-infrared range.^{26,27} Nonetheless, there has been limited discussion or investigation into the power-handling capabilities of MgO-doped TFLN modulators, particularly in the C-band.

Alternatively, thin-film lithium tantalate (TFLT), a promising candidate in integrated photonics,²⁸ offers mechanical and chemical stability comparable to TFLN, along with a similar

Received: January 18, 2025

Revised: June 20, 2025

Accepted: June 23, 2025

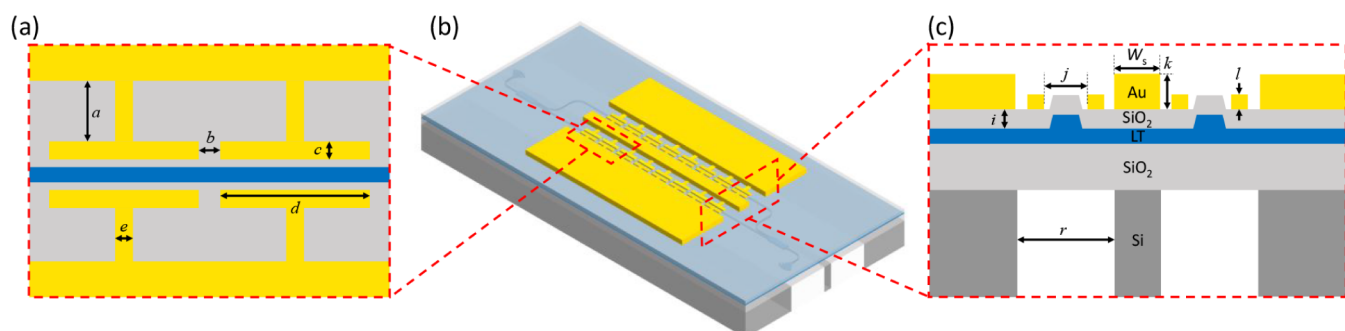


Figure 1. Proposed TFLT-based EO modulator on a Si substrate using CLTW electrodes with backside holes: (a) Detailed top-view schematic of the T-segment electrode structures. (b) Three-dimensional schematic of the EO modulator. (c) Cross-sectional schematic of the modulation section.

linear electro-optic coefficient ($r_{33} = 30.5 \text{ pm/V}$), enabling high modulation performance.²⁹ Crucially, TFLT has an optical damage threshold (2000 kW/cm²@532 nm) that is 3 orders of magnitude higher than that of LN.²⁰ This property has attracted attention in high-power nonlinear optics applications.^{20,30–32} In recent studies, different research groups observed a weak PR effect and minimal direct-current (DC) drift in TFLT-based microrings,³³ optical switches,³⁴ and modulator,³⁵ confirming the superior stability of TFLT photonic devices over TFLN.

In this paper, we designed a high-performance silicon-substrate TFLT modulator and experimentally demonstrated its stable operation at high optical power (up to 28 dBm, 630.9 mW). Compared to TFLN modulators, the TFLT modulator exhibited significantly improved stability, highlighting its higher optical damage threshold and reduced PR effect. These results underscore TFLT's potential for high-power electro-optic modulator applications.

RESULTS

Design. Figure 1 shows the three-dimensional structure of the proposed EO modulator, which employs periodic capacitively loaded traveling-wave (CLTW) electrodes on an acoustic-grade TFLT on insulator (LTOI) wafer (Novel Si Integration Technology, China). The wafer consists of a 400 nm thick TFLT layer with an X-112°Y crystal cut, a 4.7 μm thick buried oxide (BOX) layer, and a silicon substrate. The modulator's ridge waveguides have a height of 200 nm, a width of 1.5 μm, and sidewall angles of 60°. The 3 dB beam splitters/combiners are designed as multimode interference (MMI) structures. The modulation electrodes follow a CLTW design based on a classical coplanar line structure, incorporating with wide unloaded signal electrodes and periodically loaded T-segments. This design has been proven effective in achieving both large EO bandwidth and low V_π in TFLN modulators.^{6,36,37} The cross-sectional view of the modulation region is shown in Figure 1c, featuring an unloaded signal electrode width of $W_s = 80 \mu\text{m}$ and a gap $j = 1.8 \mu\text{m}$ between the opposing loaded T-segment electrodes. A 900 nm thick SiO₂ cladding layer is applied between the LT layer and metal electrodes to minimize absorption losses from the metal. The metal thicknesses for the loaded T-segment electrodes and the wide unloaded electrodes are set to $l = 200 \text{ nm}$ and $k = 1.1 \mu\text{m}$, respectively. To achieve index matching between the microwave and optical signals, the microwave refractive index is reduced through backside holes ($r = 90 \mu\text{m}$) in the silicon substrate—a robust solution for high-performance modulators

on silicon substrates.³⁷ The remaining CLTW electrode parameters are optimized for impedance matching, with dimensions $(a, b, c, d, e) = (15.3, 3, 2, 47, 5) \mu\text{m}$, as shown in Figure 1a.

We simulated the optical and electrical modes of the modulator using a multiphysics field solver based on the finite element method at a wavelength of 1550 nm and a frequency of 100 GHz. The simulated modulation efficiency, represented by the half-wave voltage-length product $V_\pi L = 2.41 \text{ V}\cdot\text{cm}$, was derived for a waveguide oriented along the Y axis of the LT crystal and for the fundamental transverse-electric (TE) mode, as shown in Figure 2a. The microwave field is concentrated in the gap between the opposing loaded T-segment electrodes (Figure 2b), resulting in strong overlap between the electrical and optical fields, which contributes to the low $V_\pi L$ value. The simulated characteristic impedance Z_c , RF effective index n_m , and RF loss α_m are shown in Figure 2c–e, respectively. The RF loss curves follow the relation $\alpha_m = \alpha_0 f^{1/2}$, where α_0 represents the frequency-independent characteristic RF loss, extracted as 0.194 dB·cm⁻¹ GHz^{-1/2}, which is comparable to that of advanced TFLN modulators.³⁷ The backside hole design effectively reduces the microwave refractive index, aligning it closely with the optical mode group index ($n_g = 2.19$). The characteristic impedance Z_c is designed to be 50 Ω. Due to the low RF loss, index matching, and impedance matching, the modulator achieves a large EO bandwidth. As shown in Figure 2f, the bandwidth roll-off is less than 1 dB at 100 GHz for a 7 mm-long device.

The designed TFLT modulator was fabricated using standard microfabrication processes (see **Methods**). By adjusting the width of backside hole, the RF effective index n_m could be fine-tuned to closely match the optical mode group index. The final fabricated modulator has a modulation length of $L = 0.7 \text{ cm}$. It is noteworthy that the waveguide is oriented along the 112° Y axis of the LT crystal, with the electric field along the 22° Z axis. Therefore, the EO efficiency is about 0.83 times that of the highest EO coefficient in the LT crystal's optimal orientation.³⁸ Figure 3a–e show some optical microscope images of the fabricated modulator, including views of the chip's backside.

Measurement and Analysis. A tunable laser combined with a preamplifier (erbium-doped fiber amplifier, EDFA) was used as the light source, followed by a polarization controller to ensure operation in the TE mode. Light was coupled into and out of the modulator using a pair of grating couplers (GCs), each with a coupling loss of 6 dB at the operating wavelength. To monitor the output power, 5% of the light was

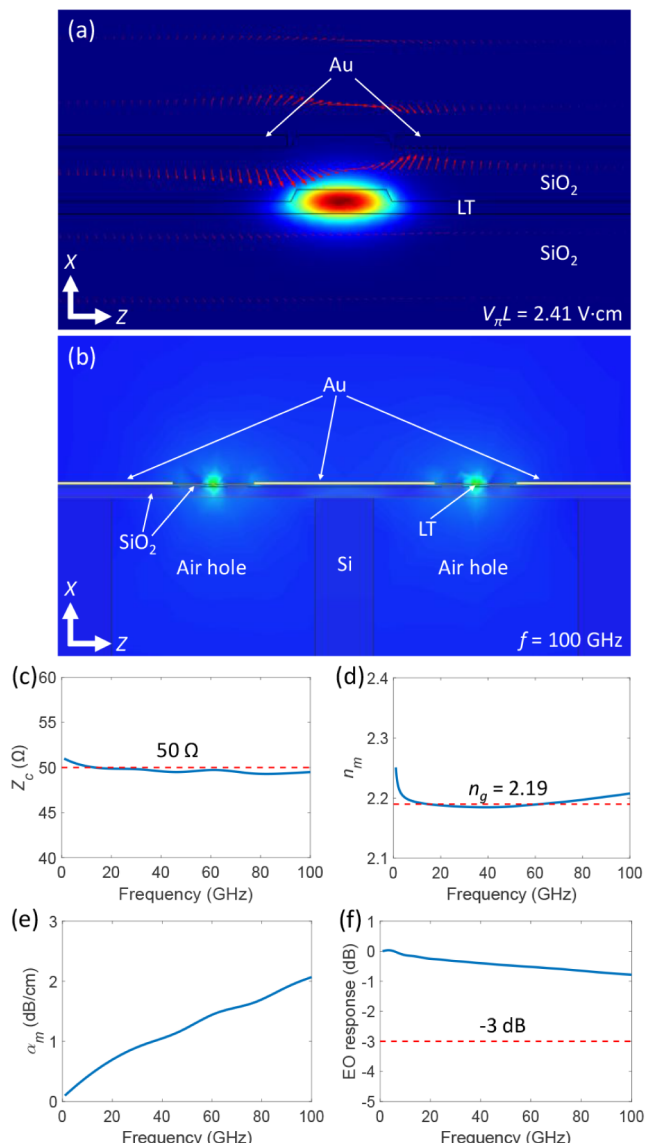


Figure 2. (a) Simulated TE optical mode profile and static electrical field distribution. (b) Simulated RF mode profile at a microwave frequency of $f = 100 \text{ GHz}$. Simulation results for (c) characteristic impedance Z_c , (d) RF effective index n_m , (e) RF loss α_m and (f) EO bandwidth. The three red dashed lines in (c), (d), and (f) represent the source/load impedance 50Ω , optical group index n_g and the -3 dB indicator line, respectively.

directed to a power meter, while the remaining 95% was sent into another EDFA to maintain consistent optical power before reaching the high-speed photodiode (PD). RF probes were employed to deliver electrical and RF signals to the modulator. The electrical responses of the modulator were measured using a vector network analyzer, as shown in Figure 3f. The EE reflection S_{11} remained below -20 dB across the entire frequency range, indicating good impedance matching. The EE transmission S_{21} exhibited a 5.7 dB roll-off at 67 GHz . Extracted values for n_m and Z_c are plotted in Figure 3g,h, respectively. The significant roll-off in S_{21} compared to simulations was primarily attributed to nonideal metal deposition and residual silicon beneath the electrodes, as indicated by the dark, slightly blurred shadows near the edge of the backside hole in Figure 3a. The blurring occurs because the microscope was focused on the electrode

surface rather than the residual silicon. Deviations in the calculated n_m from the simulated values were likely due to inaccuracies in the backside hole dimensions and the slope of the positive sidewall caused by deep silicon etching, which may have narrowed the silicon opening beneath the LT waveguide.

To measure the V_{π} of the modulator, a sawtooth wave with a peak-to-peak voltage of 20 V and a frequency of 100 kHz was applied to the electrodes. The measured V_{π} values at 0 dBm and 35 dBm optical input power (equivalent to -7 dBm and 28 dBm within the modulator, respectively) are shown in Figure 4a,b. The 35 dBm optical power was generated using a tunable laser combined with an erbium-doped fiber amplifier. The calculated $V_{\pi}L$ was $3.22 \text{ V}\cdot\text{cm}$ for both input power levels. If the modulated light propagated strictly along the Y axis of the LT crystal, the equivalent $V_{\pi}L$ would be $2.67 \text{ V}\cdot\text{cm}$, closely matching the simulated result. The insets in Figure 4a,b indicate a static extinction ratio (ER) and IL of approximately 22 and 2 dB, respectively. This loss is partially attributed to the alignment error between the electrodes and the waveguide, as the device was fabricated using a contact lithography system (EVG620). Further reduction in IL is expected with more precise alignment techniques. The small-signal EO response S_{21} was measured with a 70 GHz photodetector, as shown in Figure 4c. The 3 dB EO bandwidth was around 55 GHz for both optical power levels, primarily limited by RF losses, as shown in Figure 3f. Consistent $V_{\pi}L$, ER, loss, and EO bandwidth results were observed for both low and high optical power inputs, confirming that the high power (28 dBm in the waveguide) is well below the material's optical damage threshold.

The modulator's performance for high-speed data transmission at different optical power levels was also evaluated (see Methods). Figure 4d–g displays EO eye diagrams for on–off key (OOK) modulation at 80 Gb/s and 100 Gb/s , and four-level pulse-amplitude modulation (PAM-4) format at 80 Gb/s (40 Gbaud) and 112 Gb/s (56 Gbaud) under 0 dBm optical input power (-7 dBm within the modulator). Similar tests conducted with 35 dBm optical input power are shown in Figure 4h–k. The eye diagrams remained clear and well-opened, with slight improvement at higher optical power, likely due to enhanced signal-to-noise ratio (SNR).

To further demonstrate the high optical power operating stability of the modulator, EO eye diagram measurements for the OOK modulation format at 80 Gb/s were performed at various optical power levels within the modulator, recording dynamic ER and SNR values. For comparison, a modulator with a similar T-segment structure, fabricated on X-cut TFLN, with a coupling loss of 7 dB per grating, was tested under identical conditions. It is worth noting that a 1 dB front-end loss was introduced by the polarization controller and transmission fibers prior to the modulator input.

As shown in Figure 5a, the TFLT modulator exhibits stable ER and SNR across the entire tested optical power range. In contrast, while the TFLN modulator initially achieves slightly higher SNR at low optical powers, both its ER and SNR progressively degrade as the optical power increases, as shown in Figure 5b. The slightly lower SNR of the TFLT modulator compared to the TFLN modulator at low optical powers is likely due to its relatively lower EE bandwidth, which limits the rise/fall times and slightly reduces eye diagram clarity. The insets on the right of Figure 5 show the eye diagrams for both modulators at each power level, captured with identical sampling parameters. At powers below 21 dBm , both

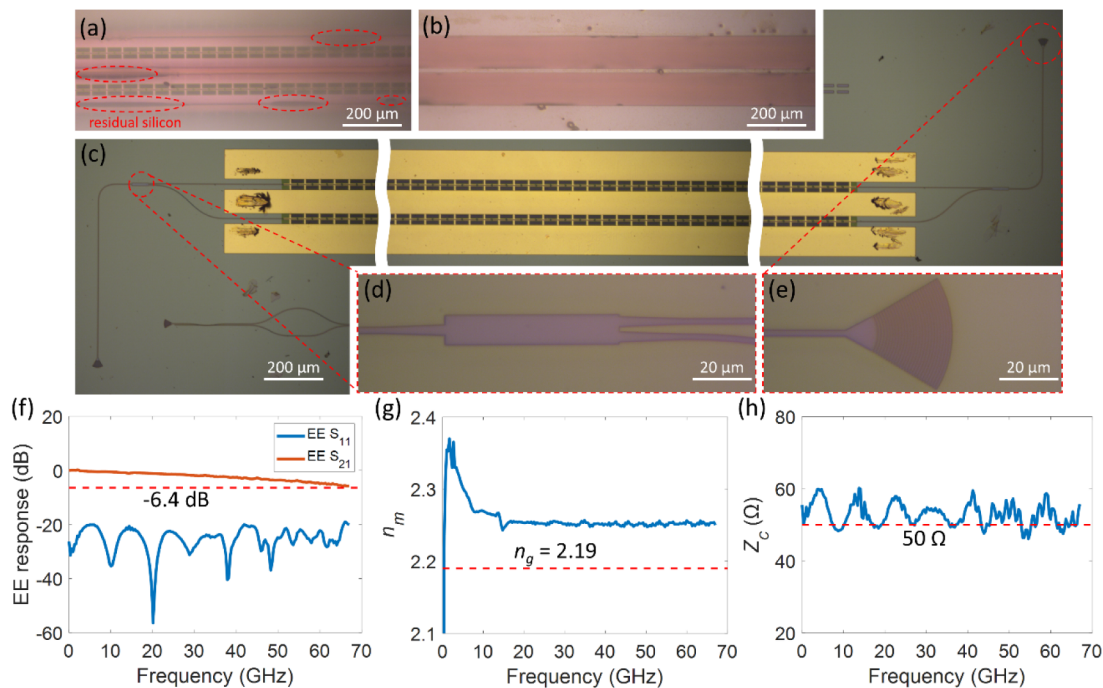


Figure 3. Backside view of the fabricated modulator, with a microscope-focused view of (a) the electrode and (b) the chip's backside surface. (c) Top view of the entire fabricated device. Detailed top views of the (d) 1×2 MMI splitter and (e) grating coupler. (f) Measured electrical reflection S_{11} and transmission S_{21} of the fabricated EO modulator. Dduced (g) RF effective index n_m , and (h) characteristic impedance Z_c . The three red dashed lines in (f), (g), and (h) represent the -6.4 dB indicator line, the optical group index n_g , and the source/load impedance $50\ \Omega$, respectively.

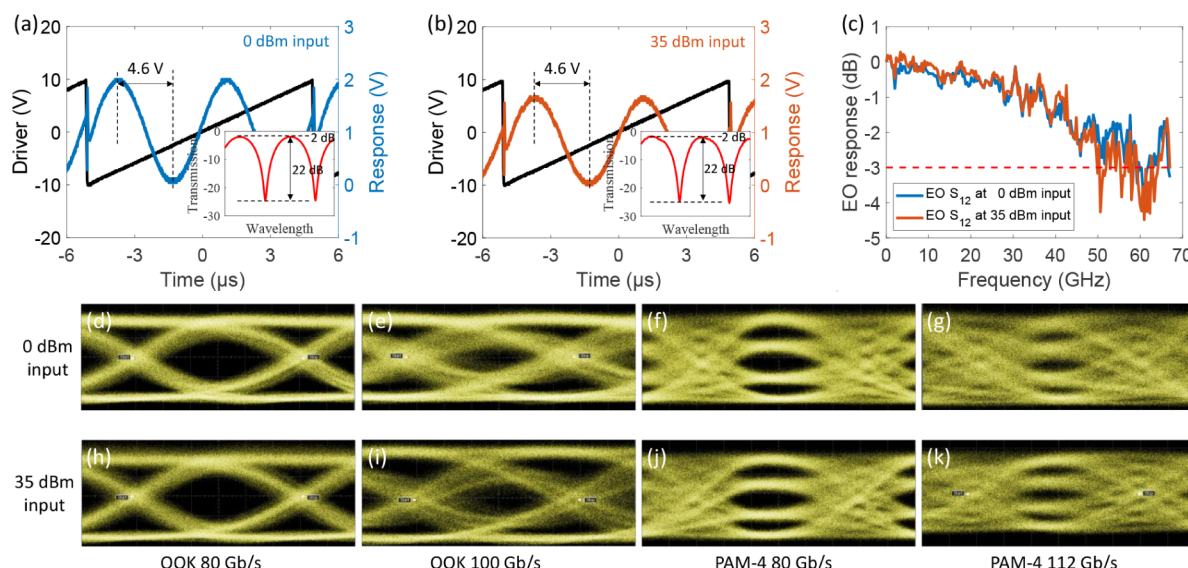


Figure 4. Measured EO response of the fabricated modulator using a 100 kHz sawtooth wave with a peak-to-peak voltage of 20 V at (a) 0 dBm and (b) 35 dBm optical input power (equivalent to -7 dBm and 28 dBm within the modulator, respectively). The V_x values are indicated. Insets display the measured normalized transmissions, showing the ILs and static ERs of the modulator for both optical input powers. (c) Measured EO bandwidth of the modulator for both optical input powers. (d–k) Measured EO eye diagrams: the first to fourth columns correspond to OOK 80Gb/s, OOK 100Gb/s, PAM-4 80 Gb/s, and PAM-4 112 Gb/s, respectively. The first row shows results for 0 dBm optical input power, while the second row shows results for 35 dBm optical input power.

modulators produce well-defined eye diagrams. However, at 27 dBm, the TFLN modulator exhibits significant eye quality degradation, including unstable crossing levels. Notably, even after resetting the operating point via wavelength tuning, the eye rapidly deteriorates—indicating an inherent instability. In contrast, the TFLT modulator maintains high-quality and consistent eye diagrams even under the highest tested optical powers.

This behavior is further reflected in the bit-error rate (BER) performance. As shown in Figure 6a, the BER of both modulators initially decreases with increasing optical power, falling below the KP-4 forward error correction threshold. With further power increase, the BER reaches a plateau. However, for the TFLN modulator, when the input exceeds $\sim 28\text{ dBm}$, the average output power no longer increases and becomes unstable (as seen in the inset of Figure 6a and in

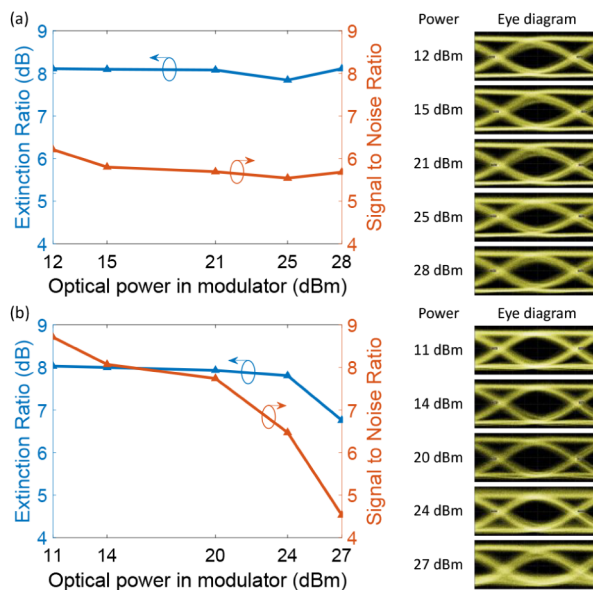


Figure 5. Dynamic ER and SNR values at various optical power levels within the modulator, along with the corresponding eye diagrams for each power point for (a) the TFLT-based modulator and (b) the TFLN-based modulator.

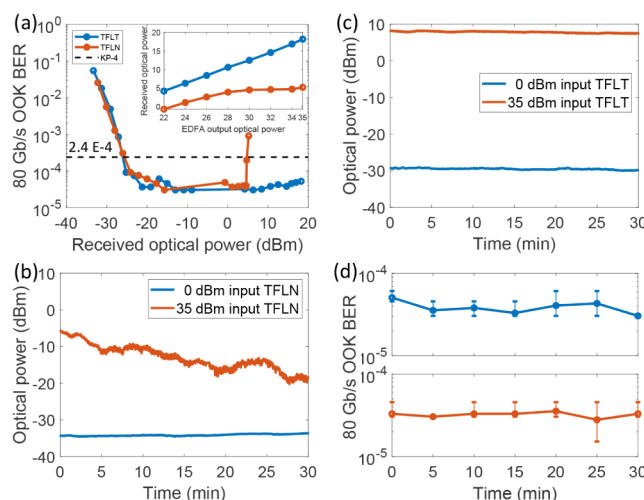


Figure 6. (a) Measured BER as a function of received optical power for 80 Gb/s OOK signals. The inset shows the correlation between the input optical power and the average modulated optical power detected at the receiver. Stability of the modulated average output optical power over time for (b) the TFLN-based and (c) the TFLT-based modulators, where a small fraction (5%) of the output is tapped for monitoring. (d) BER stability of TFLT-based modulators over time under input optical powers of 0 dBm and 35 dBm.

Figure 6b), accompanied by a noticeable rise in BER. This degradation aligns with the eye diagram deterioration discussed in Figure 5. In contrast, the TFLT modulator exhibits a linear relationship between input and output power and maintains consistently low BER even at high input powers. As shown in Figure 6c,d, the TFLT modulator demonstrates excellent temporal stability in both output power and BER over a 30 min period at input powers of 0 dBm and 35 dBm, confirming its robustness for high-power operation.

In our experiments, no DC bias was applied; instead, the operating point was adjusted by fine-tuning the wavelength, leveraging the inherent arm asymmetry of the Mach-Zehnder

interferometer (MZI). This confirms that the observed instability in the TFLN modulator originates from optical effects rather than DC drift. At high optical power, PR effects in the LN waveguide induce space-charge redistribution, leading to local refractive index variations. These distort the guided mode and can excite high-order modes,¹⁹ ultimately causing ER degradation, increased IL, and operating point instability due to index shifts in the phase shifter. In contrast, the LT waveguide exhibits significantly weaker PR effects and a higher optical damage threshold, likely due to its higher photon energy resistance,²⁸ stronger Ta–O bonds,³⁹ and lower density of vacancies and defect states.⁴⁰ Notably, stronger PR effects correspond to a lower optical damage threshold, as less optical power is required to induce substantial space-charge accumulation and refractive index modulation. The maximum input power tested for the TFLT modulator in this work was limited only by the available optical source output.

CONCLUSIONS

This paper presents a 7 mm EO modulator based on TFLT with an X-112°Y crystal cut, utilizing CLTW electrodes with backside holes. The fabricated modulator demonstrates a consistent EO bandwidth exceeding 55 GHz, a large static ER of over 20 dB, and V_{π} of 4.6 V under both 0 dBm and 35 dBm optical input powers (equivalent to -7 dBm and 28 dBm within the modulator, respectively). Successful data transmissions are achieved using OOK modulation at 100 Gb/s and PAM-4 at 112 Gb/s, under both input power levels. Compared to TFLN modulators, the TFLT modulator exhibits significantly improved stability, as evidenced by consistent ER, SNR, and BER performance under increasing optical power. Long-term stability of output power and BER measurements at high input power further confirm the device's robustness. This enhanced stability is attributed to TFLT's higher optical damage threshold and reduced PR effect, ensuring stable operation point near quadrature. These findings highlight the strong potential of TFLT modulators for next-generation high-power photonic applications, including nonlinear optics, microwave photonics, and THz communications.

METHODS

Fabrication. First, the MZI patterns were defined via electron beam lithography on a Ma-N 2403 resist, followed by inductively coupled plasma (ICP) dry etching using pure Ar⁺ gas. A series of chemical cleaning steps were employed to remove redeposition and residual resist. Next, a 900 nm thick SiO₂ cladding layer was deposited using plasma-enhanced chemical vapor deposition (PECVD). The loaded T-segment electrodes and unloaded electrodes were then deposited via electron-beam evaporation and a lift-off process. The chip was then thinned to approximately 250 μ m using grinding and polishing equipment. Backside holes were patterned, and the silicon substrate beneath the modulation section was removed using a double-side mask aligner and anisotropic deep reactive ion etching (RIE) of silicon until the BOX layer was reached.

Measurements for Eye Diagrams and BERs. An arbitrary waveform generator (Micram DAC10004) combined with a clock source (Agilent E8257D) was used to generate OOK and PAM-4 signals. The signal was amplified by an RF amplifier (SHF 807c) and fed to the device through an RF probe (GGB 67A). Another probe was used to provide an off-chip 50 Ω termination for the electrode. The modulated

optical signal was detected using a preamplified receiver, consisting of a variable optical attenuator, an erbium-doped fiber amplifier (EDFA), and a high-speed PD (Finisar BPDV3320R). The output signal was recorded using either a digital sampling oscilloscope (Agilent 81600D) for eye diagrams or a real-time oscilloscope (Tektronix 73304D) for offline digital signal processing (DSP). The offline DSP includes down-sampling, timing phase synchronization, and a 25-tap least-mean-square equalizer.

AUTHOR INFORMATION

Corresponding Authors

Changjian Guo — *Guangdong Provincial Key Laboratory of Optical Information Materials and Technology, South China Academy of Advanced Optoelectronics, South China Normal University, Guangzhou 510006, China; National Center for International Research on Green Optoelectronics, South China Normal University, Guangzhou 510006, China;*
Email: changjian.guo@coer-scnu.org

Kaixuan Chen — *Guangdong Provincial Key Laboratory of Optical Information Materials and Technology, South China Academy of Advanced Optoelectronics, South China Normal University, Guangzhou 510006, China; National Center for International Research on Green Optoelectronics, South China Normal University, Guangzhou 510006, China;*
orcid.org/0000-0002-2538-6793; Email: chenkaixuan@m.scnu.edu.cn

Liu Liu — *State Key Laboratory of Extreme Photonics and Instrumentation, College of Optical Science and Engineering, International Research Center for Advanced Photonics, Zhejiang University, Hangzhou 310058, China;*
orcid.org/0000-0002-3651-544X; Email: liuliuopt@zju.edu.cn

Authors

Haohua Wang — *Guangdong Provincial Key Laboratory of Optical Information Materials and Technology, South China Academy of Advanced Optoelectronics, South China Normal University, Guangzhou 510006, China*

Ao Cui — *Guangdong Provincial Key Laboratory of Optical Information Materials and Technology, South China Academy of Advanced Optoelectronics, South China Normal University, Guangzhou 510006, China*

Bin Chen — *State Key Laboratory of Extreme Photonics and Instrumentation, College of Optical Science and Engineering, International Research Center for Advanced Photonics, Zhejiang University, Hangzhou 310058, China*

Ziliang Ruan — *State Key Laboratory of Extreme Photonics and Instrumentation, College of Optical Science and Engineering, International Research Center for Advanced Photonics, Zhejiang University, Hangzhou 310058, China*

Complete contact information is available at:
<https://pubs.acs.org/10.1021/acsphtnics.5c00159>

Funding

National Natural Science Foundation of China (62135012), Leading Innovative and Entrepreneur Team Introduction Program of Zhejiang (2021R01001), Basic and Applied Basic Research Foundation of Guangdong Province (2024A1515011710), and Guangdong Provincial Key Laboratory of Optical Information Materials and Technology (2023B1212060065).

Notes

The authors declare no competing financial interest.

REFERENCES

- (1) Zhu, D.; Shao, L.; Yu, M.; Cheng, R.; Desiatov, B.; Xin, C. J.; Hu, Y.; Holzgrafe, J.; Ghosh, S.; Shams-Ansari, A.; Puma, E.; Sinclair, N.; Reimer, C.; Zhang, M.; Lončar, M. Integrated photonics on thin-film lithium niobate. *Adv. Opt. Photon.* **2021**, *13* (2), 242–352.
- (2) Li, Y.; Sun, M.; Miao, T.; Chen, J. Towards High-Performance Pockels Effect-Based Modulators: Review and Projections. *Micro-machines* **2024**, *15* (7), 865.
- (3) Wang, C.; Zhang, M.; Stern, B.; Lipson, M.; Lončar, M. Nanophotonic lithium niobate electro-optic modulators. *Opt. Express* **2018**, *26* (2), 1547–1555.
- (4) Yang, F.; Fang, X.; Chen, X.; Zhu, L.; Zhang, F.; Chen, Z.; Li, Y. Monolithic thin film lithium niobate electro-optic modulator with over 110 GHz bandwidth. *Chin. Opt. Lett.* **2022**, *20* (2), 022502.
- (5) Xu, M.; Zhu, Y.; Pittalá, F.; Tang, J.; He, M.; Ng, W. C.; Wang, J.; Ruan, Z.; Tang, X.; Kuschnerov, M.; Liu, L.; Yu, S.; Zheng, B.; Cai, X. Dual-polarization thin-film lithium niobate in-phase quadrature modulators for terabit-per-second transmission. *Optica* **2022**, *9* (1), 61–62.
- (6) Chen, G.; Chen, K.; Gan, R.; Ruan, Z.; Wang, Z.; Huang, P.; Lu, C.; Lau, A. P. T.; Dai, D.; Guo, C.; Liu, L. High performance thin-film lithium niobate modulator on a silicon substrate using periodic capacitively loaded traveling-wave electrode. *APL Photonics* **2022**, *7* (2), 026103.
- (7) Boes, A.; Chang, L.; Langrock, C.; Yu, M.; Zhang, M.; Lin, Q.; Lončar, M.; Fejer, M.; Bowers, J.; Mitchell, A. Lithium niobate photonics: Unlocking the electromagnetic spectrum. *Science* **2023**, *379* (6627), No. eabj4396.
- (8) Ivankovski, Y.; Mendlovic, D. High-rate–long-distance fiber-optic communication based on advanced modulation techniques. *Appl. Opt.* **1999**, *38* (26), 5533–5540.
- (9) Sun, D.; Zhang, Y.; Wang, D.; Song, W.; Liu, X.; Pang, J.; Geng, D.; Sang, Y.; Liu, H. Microstructure and domain engineering of lithium niobate crystal films for integrated photonic applications. *Light: sci. Appl.* **2020**, *9* (1), 197.
- (10) Marpaung, D.; Yao, J.; Capmany, J. Integrated microwave photonics. *Nat. Photonics* **2019**, *13* (2), 80–90.
- (11) Feng, H.; Ge, T.; Guo, X.; Wang, B.; Zhang, Y.; Chen, Z.; Zhu, S.; Zhang, K.; Sun, W.; Huang, C.; Yuan, Y.; Wang, C. Integrated lithium niobate microwave photonic processing engine. *Nature* **2024**, *627* (8002), 80–87.
- (12) Burla, M.; Hoessbacher, C.; Heni, W.; Haffner, C.; Fedoryshyn, Y.; Werner, D.; Watanabe, T.; Massler, H.; Elder, D. L.; Dalton, L. R.; Leuthold, J. 500 GHz plasmonic Mach-Zehnder modulator enabling sub-THz microwave photonics. *APL Photonics* **2019**, *4* (5), 056106.
- (13) Feng, H.; Zhang, K.; Sun, W.; Ren, Y.; Zhang, Y.; Zhang, W.; Wang, C. Ultra-high-linearity integrated lithium niobate electro-optic modulators. *Photon. Res.* **2022**, *10* (10), 2366–2373.
- (14) Cox, C. H., *Analog Optical Links: Theory And Practice*; Cambridge University Press, 2006.
- (15) Glass, A. The Photorefractive Effect. *Opt. Eng.* **1978**, *17* (5), 175470.
- (16) Xu, Y.; Shen, M.; Lu, J.; Surya, J. B.; Sayem, A. A.; Tang, H. X. Mitigating photorefractive effect in thin-film lithium niobate microring resonators. *Opt. Express* **2021**, *29* (4), 5497–5504.
- (17) Celik, O. T.; Yousry Ammar, N.; Park, T.; Stokowski, H. S.; Multani, K. K. S.; Hwang, A. Y.; Gyger, S.; Guo, Y.; Fejer, M. M.; Safavi-Naeini, A. H. Roles of temperature, materials, and domain inversion in high-performance, low-bias-drift thin film lithium niobate blue light modulators. *Opt. Express* **2024**, *32* (21), 36160–36170.
- (18) Kong, Y.; Bo, F.; Wang, W.; Zheng, D.; Liu, H.; Zhang, G.; Rupp, R.; Xu, J. Recent Progress in Lithium Niobate: Optical Damage, Defect Simulation, and On-Chip Devices. *Adv. Mater.* **2020**, *32* (3), 1806452.
- (19) Villarroel, J.; Carnicer, J.; Luedtke, F.; Carrascosa, M.; García-Cabañas, A.; Cabrera, J. M.; Alcazar, A.; Ramiro, B. Analysis of

- photorefractive optical damage in lithium niobate: application to planar waveguides. *Opt. Express* **2010**, *18* (20), 20852–20861.
- (20) Xue, M.; Yan, X.; Wu, J.; Ge, R.; Yuan, T.; Chen, Y.; Chen, X. On-chip ultraviolet second-harmonic generation in lithium-tantalate thin film microdisk. *Chin. Opt. Lett.* **2023**, *21* (6), 061902.
- (21) Zhang, M.; Wang, C.; Kharel, P.; Zhu, D.; Lončar, M. Integrated lithium niobate electro-optic modulators: when performance meets scalability. *Optica* **2021**, *8* (5), 652–667.
- (22) Valdez, F.; Mere, V.; Wang, X.; Boynton, N.; Friedmann, T. A.; Arterburn, S.; Dallo, C.; Pomerene, A. T.; Starbuck, A. L.; Trotter, D. C.; Lentine, A. L.; Mookherjea, S. 110 GHz, 110 mW hybrid silicon-lithium niobate Mach-Zehnder modulator. *Sci. Rep.* **2022**, *12* (1), 18611.
- (23) Kong, Y.; Liu, S.; Xu, J. Recent Advances in the Photorefraction of Doped Lithium Niobate Crystals. *Materials* **2012**, *5* (10), 1954–1971.
- (24) Schwesyg, J. R.; Falk, M.; Phillips, C. R.; Jundt, D. H.; Buse, K.; Fejer, M. M. Pyroelectrically induced photorefractive damage in magnesium-doped lithium niobate crystals. *J. Opt. Soc. Am. B* **2011**, *28* (8), 1973–1987.
- (25) Furukawa, Y.; Kitamura, K.; Takekawa, S.; Miyamoto, A.; Terao, M.; Suda, N. Photorefraction in LiNbO₃ as a function of [Li]/[Nb] and MgO concentrations. *Appl. Phys. Lett.* **2000**, *77* (16), 2494–2496.
- (26) Valdez, F.; Mere, V.; Mookherjea, S. 100 GHz bandwidth, 1 V integrated electro-optic Mach-Zehnder modulator at near-IR wavelengths. *Optica* **2023**, *10* (5), 578–584.
- (27) Celik, O. T.; Ammar, N. Y.; Stokowski, H.; Park, T.; Safavi-Naeini, A. In *Visible Electro-optic Modulator Array in Thin-Film Lithium Niobate for Atomic Qubit Control*. In *Frontiers In Optics + Laser Science 2023 (Fio, LS)*; Optica Publishing Group: Tacoma, WA, 2023. .
- (28) Wang, C.; Li, Z.; Riemensberger, J.; Lihachev, G.; Churaev, M.; Kao, W.; Ji, X.; Zhang, J.; Blesin, T.; Davydova, A.; Chen, Y.; Huang, K.; Wang, X.; Ou, X.; Kippenberg, T. J. Lithium tantalate photonic integrated circuits for volume manufacturing. *Nature* **2024**, *629* (8013), 784–790.
- (29) Wang, C.; Fang, D.; Zhang, J.; Kotz, A.; Lihachev, G.; Churaev, M.; Li, Z.; Schwarzenberger, A.; Ou, X.; Koos, C.; Kippenberg, T. J. Ultrabroadband thin-film lithium tantalate modulator for high-speed communications. *Optica* **2024**, *11* (12), 1614–1620.
- (30) Yan, X.; Liu, Y. A.; Ge, L.; Zhu, B.; Wu, J.; Chen, Y.; Chen, X. High optical damage threshold on-chip lithium tantalate microdisk resonator. *Opt. Lett.* **2020**, *45* (15), 4100–4103.
- (31) Nishi, H.; Tsuchizawa, T.; Segawa, T.; Matsuo, S. In *Low-loss lithium tantalate on insulator waveguide towards on-chip nonlinear photonics*, 2022. In *2022 International Conference on Photonics in Switching and Computing (PSC)*; IEEE: 2022, pp 1–3.
- (32) Senouci, K.; Mansour, D.; Abderrahmane, A. Electro-optic properties of one-dimensional (1D) nonlinear perfect photonic crystals based on Lithium tantalate layer. *Optik* **2022**, *265*, 169537.
- (33) Yu, J.; Ruan, Z.; Xue, Y.; Wang, H.; Gan, R.; Gao, T.; Guo, C.; Chen, K.; Ou, X.; Liu, L. Tunable and stable micro-ring resonator based on thin-film lithium tantalate. *APL Photonics* **2024**, *9* (3), 036115.
- (34) Wang, H.; Xing, X.; Ruan, Z.; Yu, J.; Chen, K.; Ou, X.; Liu, L. Optical switch with an ultralow DC drift based on thin-film lithium tantalate. *Opt. Lett.* **2024**, *49* (18), 5019–5022.
- (35) Powell, K.; Li, X.; Assumpcao, D.; Magalhães, L.; Sinclair, N.; Lončar, M. DC-stable electro-optic modulators using thin-film lithium tantalate. *Opt. Express* **2024**, *32* (25), 44115–44122.
- (36) Wang, Z.; Chen, G.; Ruan, Z.; Gan, R.; Huang, P.; Zheng, Z.; Lu, L.; Li, J.; Guo, C.; Chen, K.; Liu, L. Silicon–Lithium Niobate Hybrid Intensity and Coherent Modulators Using a Periodic Capacitively Loaded Traveling-Wave Electrode. *ACS Photonics* **2022**, *9* (8), 2668–2675.
- (37) Wang, M.; Qi, L.; Wang, H.; Ruan, Z.; Chen, G.; Chen, B.; Gong, S.; Chen, K.; Liu, L. Robust thin-film lithium niobate modulator on a silicon substrate with backside holes. *Chin. Opt. Lett.* **2024**, *22* (5), 050601.
- (38) Bahadori, M.; Goddard, L. L.; Gong, S. Fundamental electro-optic limitations of thin-film lithium niobate microring modulators. *Opt. Express* **2020**, *28* (9), 13731–13749.
- (39) Gruber, M.; Konetschnik, R.; Popov, M.; Spitaler, J.; Supancic, P.; Kiener, D.; Bermejo, R. Atomistic origins of the differences in anisotropic fracture behaviour of LiTaO₃ and LiNbO₃ single crystals. *Acta Mater.* **2018**, *150*, 373–380.
- (40) Grachev, V. G.; Malovichko, G. I. Structures of Impurity Defects in Lithium Niobate and Tantalate Derived from Electron Paramagnetic and Electron Nuclear Double Resonance Data. *Crystals* **2021**, *11* (4), 339.